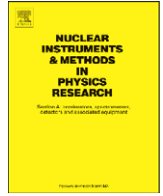




Contents lists available at ScienceDirect

Nuclear Instruments and Methods in Physics Research A

journal homepage: www.elsevier.com/locate/nima

Performance of the prototype module of the GlueX electromagnetic barrel calorimeter

B.D. Leverington^a, G.J. Lolos^a, Z. Papandreou^{a,*}, R. Hakobyan^a, G.M. Huber^a, K.L. Janzen^a, A. Semenov^a, E.B. Scott^b, M.R. Shepherd^b, D.S. Carman^c, D.W. Lawrence^c, E.S. Smith^c, S. Taylor^c, E.J. Wolin^c, F.J. Klein^d, J.P. Santoro^d, D.I. Sober^d, C. Kourkoumeli^e

^a Department of Physics, University of Regina, Regina, SK, Canada, S4S 0A2

^b Department of Physics, Indiana University, Bloomington, IN 47405, USA

^c Thomas Jefferson National Accelerator Facility, Newport News, VA 23606, USA

^d Department of Physics, The Catholic University of America, Washington, DC 20064, USA

^e Department of Physics, National and Kapodistrian University of Athens, 157 84 Athens, Greece

ARTICLE INFO

Article history:

Received 12 June 2008

Received in revised form

13 August 2008

Accepted 15 August 2008

Available online 3 September 2008

Keywords:

Electromagnetic calorimeter

Scintillating fibres

ABSTRACT

A photon beam test of the 4 m long prototype lead/scintillating-fibre module for the GlueX electromagnetic barrel calorimeter was carried out in Hall B at the Thomas Jefferson National Accelerator Facility with the objective of measuring the energy and timing resolutions of the module as well as the number of photoelectrons generated. Data were collected over an energy range of 150–650 MeV at multiple positions and angles along the module. Details of the analysis at the centre of and perpendicular to the module are shown herein; the results are $\sigma_E/E = 5.4\%/\sqrt{E(\text{GeV})} \oplus 2.3\%$, $\sigma_{\Delta T/2} = 70/\sqrt{E}$ ps, and 660 photoelectrons for 1 GeV at each end of the module.

© 2008 Elsevier B.V. All rights reserved.

1. Introduction

The principal aim behind the GlueX experiment is to elucidate the phenomenon of confinement, by conducting advanced meson spectroscopy and searching for predicted exotic hybrid states with explicit gluonic degrees of freedom. Such states have a plethora of decays leading to photons in the final state, and require hermetic calorimetry for their detection and measurement of their four-momentum. Test results from the cylindrical electromagnetic calorimeter for GlueX are reported herein.

A brief overview of the GlueX experiment is presented in Section 2. The photon beam test—conducted in Hall B at the Thomas Jefferson National Accelerator facility—and the setup of the experiment are covered in Section 3. The analysis method and results for the energy resolution of the Hall-B beam test are described in Section 4. The timing resolution analysis and results are shown in Section 5, while the photoelectron analysis is provided in Section 6. Lastly, the results are summarized in Section 7.

2. Overview of GlueX

To achieve the primary physics goal of GlueX, namely mapping the spectrum of gluonic excitations of light mesons, it is essential to measure photons and charged particles with sufficient acceptance and resolution to identify exclusive reactions, a requirement imposed by the amplitude analysis needed to determine the J^{PC} quantum numbers of the produced mesons. The photons of particular interest are those resulting from $\pi^0 \rightarrow \gamma\gamma$ and $\eta \rightarrow \gamma\gamma$ decays. Photoproduction data at 9 GeV are sparse and mainly come from bubble chamber experiments, in which reconstruction of final states with multiple neutral particles is impossible. Such final states are expected to make up 60% of the photoproduction cross-section, underscoring both the need and discovery potential for neutral particle reconstruction. GlueX will run in a dedicated experimental hall (Hall D) at Jefferson Lab, to be constructed as part of the 12 GeV upgrade to the lab.

2.1. The GlueX detector and barrel calorimeter

The GlueX detector design is ideally suited for a fixed-target photoproduction experiment. The 2.2 T solenoidal magnetic field traps low-energy electromagnetic background (e^+e^- pairs) generated in the target inside a small diameter beam hole that runs through the detector. The photon beam is incident on a 30-cm LH₂

* Corresponding author. Tel.: +1306 585 5379; fax: +1306 585 5659.
E-mail address: zisis@uregina.ca (Z. Papandreou).

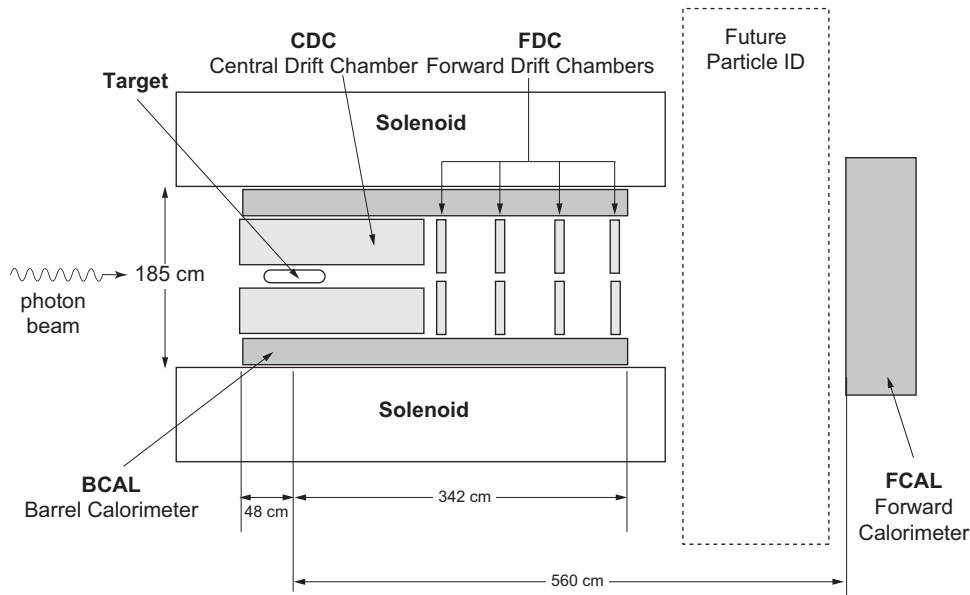


Fig. 1. Schematic of the GlueX detector. The detector has cylindrical symmetry about the beam direction. The detector subsystems and the dashed lines at angles (with respect to the beam direction) 10.8–126.4° are referenced in the text. The start counter is not shown for clarity.

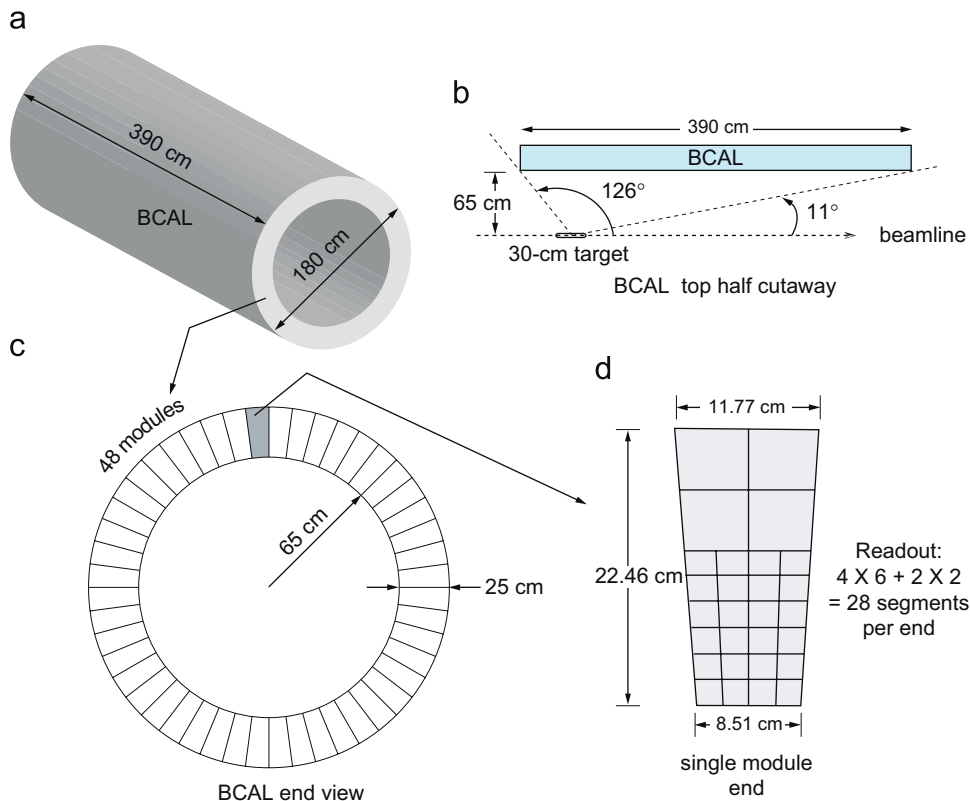


Fig. 2. The GlueX BCAL. (a) BCAL schematic; (b) a BCAL module side view; (c) end view of the BCAL showing all 48 modules and (d) an end view of a module showing read-out segmentation. Details are given in the text.

target. The target is surrounded by a start counter made of plastic scintillator that provides event timing information, a cylindrical tracking chamber (CDC) and a cylindrical electromagnetic calorimeter (BCAL). Downstream of the target are circular planar tracking chambers (FDC) and a circular planar electromagnetic calorimeter (FCAL). A schematic of the detector is shown in Fig. 1; the two electromagnetic calorimeters are used to detect and

determine the four-momentum of the aforementioned decay photons.

The BCAL is shown schematically in Fig. 2. The dimensions of this calorimeter are driven by the volume required for charged particle tracking and the bore dimensions of the solenoidal magnet. The BCAL design is based on that of the electromagnetic calorimeter used in the KLOE experiment at DAΦNE-Frascati,

which also operated in a solenoidal magnetic field [1–3]. The BCAL and KLOE calorimeters both employ a lead/scintillating-fibre (Pb/SciFi) matrix of similar length with photosensors at either end to provide energy (ADC) and time (TDC) measurements. The diameter of the KLOE calorimeter is about three times that of the BCAL.

The relevant parameters that determine the π^0 and η mass resolutions are the photon energy (E) and the polar and azimuthal position resolutions (σ_θ and σ_ϕ). The energy resolution (σ_E) depends on the number of photoelectrons (N_{pe}) yielded by the photosensors, based on the collected light. The photoelectron statistics are strongly dependent on the stochastic fluctuations of the energy deposited by the electromagnetic shower in the scintillating fibres of the calorimeter modules. In addition, the number of photoelectrons collected depends on the fraction of photon shower energy deposited in the fibres, the efficiency with which the resulting scintillation light is captured in and transmitted down the fibre to the photosensor, and the photon detection efficiency of the photosensor. The photon position is determined by the read-out segmentation in the azimuthal direction and the difference in arrival time (ΔT) of the scintillation light between the two ends of the barrel. The resolution in the time difference ($\sigma_{\Delta T}$), and therefore the polar angle resolution, also depend on the number of photoelectrons. The former is a critical input into the momentum resolution for photons and for the particle identification for charged particles, in conjunction with trajectories from the drift chambers. As such, the time difference analysis is reported in this paper as being more representative of the intrinsic BCAL resolution and independent of any external timing reference. Other parameters of relevance for extracting physics are adequate segmentation to avoid multiple occupancy, good linearity and a sufficiently low-energy threshold for photon detection.

The performance metrics for these quantities were set by simulating hadronic photoproduction at GlueX energies using PYTHIA [4] and also by simulating several of the signature reactions expected to yield exotic mesons. These studies included a GEANT-based simulation [5] of the entire GlueX detector response, including detector material and cabling, photon reconstruction and kinematic fitting. The PYTHIA simulations indicate that 70% of the produced photons with energies up to about 2 GeV will be incident on the BCAL. The photon population in the BCAL for one of the signature reactions, $\gamma p \rightarrow \eta \pi^0 p \rightarrow 4\gamma p$, where the distribution in $\eta \pi^0$ mass was uniform from 1.0 to 2.0 GeV/ c^2 and uniform in decay angles, is shown in Fig. 3. The distribution of photons is plotted as a function of position from the upstream end of the BCAL; the photons predominantly populate the downstream end of the BCAL. The target occupies the region $z = 33\text{--}63$ cm. Also shown is the average energy as a function of z with higher energy photons being more forward. The integrated thickness of the BCAL matrix, in number of radiation lengths, traversed by photons incident at various positions along the length of the BCAL is also shown. Note that there is a narrow ($\sim 1^\circ$) angular range near 11° where the photon trajectory intercepts a small number of radiation lengths of the Pb/SciFi matrix. Photons with angles less than 10° , with respect to the beam direction, are detected in the FCAL.

Moreover, the segmentation shown in Fig. 2d leads to double-occupancy in less than 1% of events with two or more photons incident on the BCAL. This segmentation is also required for adequate determination of the azimuthal angle of tracks as well as for providing information on the energy deposition profile in depth, for good cluster identification. Additionally, studies of the lowest energy photons in high-multiplicity reactions that are expected to yield exotic hybrids such as $\gamma p \rightarrow b_1(1235)\pi n \rightarrow 2\pi^+\pi^-\pi^0 n$ indicate that an energy threshold of 40 MeV suffices.

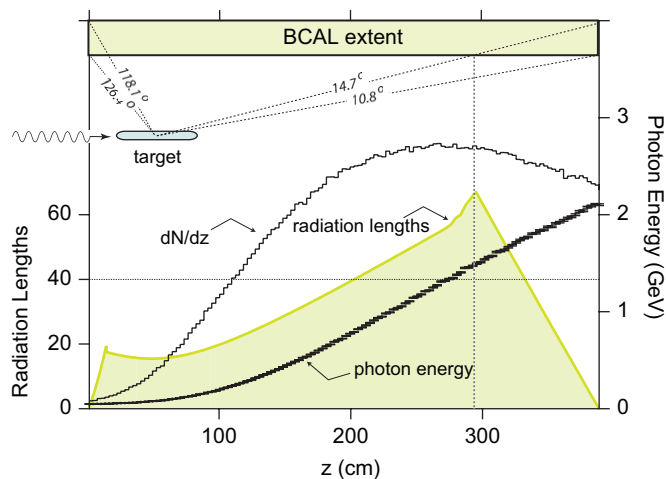


Fig. 3. The distribution of photons, their energy and integrated path length through the Pb/SciFi matrix as a function of position along the length of the BCAL for one of the GlueX signature reactions, $\gamma p \rightarrow \eta \pi^0 p \rightarrow 4\gamma p$, is shown. The target position and angular range subtended by the BCAL are also presented.

Finally, it is important to point out differences in the GlueX and KLOE applications of barrel calorimetry. KLOE is a symmetric colliding beam experiment with the intersection region at the centre of its barrel calorimeter. As a result, that calorimeter is illuminated symmetrically and nearly uniformly by photons having energies, on average, between 100 and 200 MeV and with very few photons greater than 400 MeV. On the other hand, GlueX is a fixed target experiment, resulting in a highly asymmetric photon distribution: 30% of the photons in the BCAL will have energies considerably higher than 500 MeV. Despite these differences, the KLOE experience provides valuable guidance in the design and construction of the BCAL. The achieved KLOE resolutions [3] of $\sigma_E/E = 5.4\%/ \sqrt{E(\text{GeV})}$ and $56/\sqrt{E(\text{GeV})}$ ps are also adequate to achieve the GlueX physics requirements, as indicated by our simulation studies. The extracted resolutions are a direct result of the internal Pb/SciFi matrix geometry such that similar resolutions should be expected for the BCAL [6].

2.2. Module geometry

Table 1 summarizes the salient features of the BCAL. These parameters are based on the KLOE experience, detailed GEANT-based simulations and tests of a full-scale prototype with charged particles, photon beam and cosmic rays. Aside from the attenuation length, the SciFi parameters are not brand specific but rather represent the generic parameters of double-clad fibres. The latter have a higher capture ratio compared to single clad fibres, such as used in KLOE. The nominal increase in capture ratio is over 50%, thus resulting in a similar increase in the number of photoelectrons, which can be important for low-energy photons incident on the BCAL and the corresponding thresholds of the detector.

The first prototype module (Module 1), used in the beam test described in this paper, was constructed of alternating layers of 99.98% pure lead of 0.5 mm thickness that were grooved (“swaged”), creating channels to accommodate the fibres. This was accomplished by passing the lead sheets between the two grooved rollers of a custom-designed machine thereby creating the channels by plastic deformation of the lead. The fibres were obtained from PolHiTech¹ and are type PHT-0044 double-clad

¹ PolHiTech SRL, 67061 Carsoli (AQ), Italy (www.polhitech.it).

Table 1
BCAL properties

Property	Value	Ref.
Number of modules ^a	48	
Module length ^a	390 cm	
Module inner cord ^a	8.51 cm	
Module outer cord ^a	11.77 cm	
Module thickness ^a	22.5 cm	
Module azimuthal bite ^a	7.5°	
Radial fibre pitch ^b	1.22 mm	
Azimuthal fibre pitch ^b	1.35 mm	
Lead sheet thickness ^c	0.5 mm	
Fibre diameter ^c	1.0 mm	[7]
First cladding thickness ^c	0.03 mm	[7]
Second cladding thickness ^c	0.01 mm	[7]
Core fibre refractive index ^c	1.60	[7]
First cladding refractive index ^c	1.49	[7]
Second cladding refractive index ^c	1.42	[7]
Trapping efficiency ^{c,d,e}	5.3% (min) 10.6% (max)	[7–9]
Attenuation length ^b	(307 ± 12) cm	[10]
Effective speed of light ^b , c_{eff}	(16.2 ± 0.4) cm/ns	[10]
Volume ratios ^b	37:49:14 (Pb:SF:Glue)	[11]
Effective mass number ^e	179.9	[11]
Effective atomic number ^e	71.4	[11]
Effective density ^e	4.88 g/cm ³	[11]
Sampling fraction ^f	0.125	[12]
Radiation length ^e	7.06 g/cm ² or 1.45 cm	[11]
Number of radiation lengths ^e	15.5X ₀ (total thickness)	[11]
Critical energy ^e	11.02 MeV (8.36 MeV)	[13,14]
Location of shower maximum ^e	5.0X ₀ (5.3X ₀) at 1 GeV	[13,14]
Thickness for 95% containment ^e	20.3X ₀ (20.6X ₀) at 1 GeV	[13,14]
Molière radius ^e	17.7 g/cm ² or 3.63 cm	[14]
Energy resolution ^b , σ_E/E	5.4%/√E ⊕ 2.3%	
Time difference res. ^b , $\sigma_{\Delta T/2}$	70 ps/√E	
z-position resolution ^b , σ_z	1.1 cm/√E (weighted)	
Azimuthal angle resolution ^f	~8.5 mrad	
Polar angle resolution ^f	~8 mrad	

The number of radiation lengths as well as the resolutions in the table are all at $\theta = 90^\circ$ incidence.

^a Design parameters of the BCAL specified for the final detector.

^b Quantities that have been measured.

^c Specifications from the manufacturer.

^d From literature.

^e Parameter calculated from known quantities.

^f Parameter estimated from simulations.

scintillating fibres of 1 mm diameter. These were bonded in the lead channels with Bicon-600² optical epoxy. The thickness of the module is 23 cm, its length is 400 cm and the width is 12 cm with the internal matrix geometry as indicated in Fig. 4. The matrix was built upon an aluminum base plate of 2.54 cm thickness that was further supported by a steel I-beam for added stiffness and ease of handling. Module 1 was not machined along its long sides at the 7.5° indicated in Fig. 2 and retained its rectangular profile from production. In contrast, the two ends of the module, where the read-out system was attached, were machined and polished. Visual inspection revealed that only eight of the approximately 17 000 fibres had been damaged in handling and construction. No optical defects affecting light transmission were observed in the other fibres.

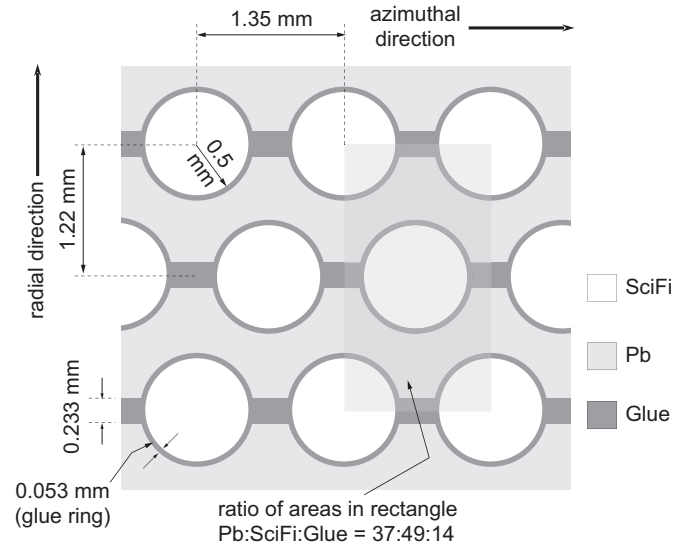


Fig. 4. The BCAL fibre matrix showing the placement of 1 mm diameter fibres in the azimuthal and radial directions. The dimensions of the azimuthal and radial pitch, the glue box between the lead sheets and the glue ring around the fibres were determined from the prototype module using a measuring microscope. Particle tracks would appear to enter the matrix from the bottom. More details are given in Ref. [11].

3. Beam test

The goals of the beam test were to measure the energy, timing and position resolutions of the prototype BCAL module as well as the response of the module at different positions along its length and at various angles of the incident beam. Results of this beam test will anchor further Monte Carlo simulations of the GlueX detector and will aid in the development of the 48 modules for the full BCAL detector. The detailed analysis and results reported in this paper are for Module 1 perpendicular to the beam ($\theta = 90^\circ$) with the beam incident at its centre ($z = 0$ cm).

3.1. Experimental facility

The beam test took place in the downstream alcove of Hall B at the Thomas Jefferson National Accelerator Facility (Jefferson Lab). In order to accommodate the module with its support frame, read-out system and cables, an additional platform was installed in front of the alcove. This expanded space allowed for the measurements with the photon beam perpendicular to the module, as well as providing a greater range of lateral and rotational degrees of freedom for the module when positioned inside the alcove. However, as illustrated in Fig. 5, the relative dimensions of the alcove and platform, with respect to the length of the module, still allowed for only a limited range of positions and incident angles that could be illuminated by the beam. Measurements, when the module was on the platform and oriented perpendicularly to the beam, were possible for relative positions of the beam spot between -100 to $+25$ cm with respect to the centre of the module. Within the alcove, the angular range was limited to angles 40° and less, and a length scan was carried out between -190 to -15 cm. The module was mounted on a cart that could be remotely rotated with good precision to the required angle. Lateral movements of the module with respect to the beam required a hall access for manual positioning.

The primary electron beam energy from the CEBAF accelerator at Jefferson Lab was $E_0 = 675$ MeV and the current was 1 nA for most of the measurements. The electron beam was incident on a

² Saint-Gobain Crystals & Detectors, USA (www.bicon.com).

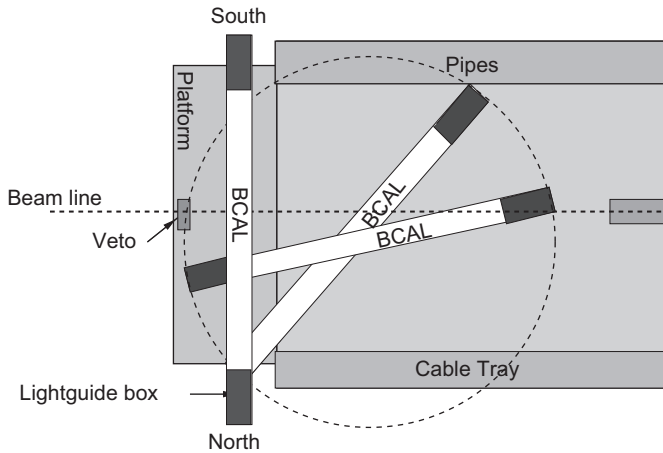


Fig. 5. Diagram of the Hall-B downstream alcove with schematic placements of the BCAL module. The drawing is not to scale.

thin target (the “radiator”) located just upstream of the magnetic spectrometer (the “tagger”). The energies of the electrons scattered from the radiator were measured, thus providing timing and momentum information for the associated bremsstrahlung photons with a spectrum of energies from 150 up to 650 MeV, as described below. The photon beam was collimated with a 2.6 mm collimator reducing the flux after collimation to 6.5% of its original value, resulting in a beam spot of virtually uniform density with a diameter of 1.9 cm on the BCAL module. The distance from the radiator to the collimator and the collimator to the BCAL were 5.8 and ~39 m, respectively.

The Hall-B tagger system determines the electron momentum information from 384 individual scintillator paddles, called E-counters, with a phototube on one end. Each of these counters is arranged to cover constant momentum intervals of $0.003E_0$ and to physically overlap with its adjacent neighbour by $\frac{1}{3}$ of its width, thus creating 767 individual photon energy bins and providing an energy resolution of $0.001E_0$. The timing information, on the other hand, is provided by 61 individual scintillator counters, called T-counters, with phototubes attached to both ends. The T-counters are classified in two groups. The first 19 (narrower) counters cover 75–90% of the incident electron energy range and the remaining 42 counters cover the 20–75% range. See Ref. [15] for more details on the Hall-B tagger.

3.2. Read-out and electronics

The module was divided into 18 read-out segments, each with dimensions $3.81 \times 3.81 \text{ cm}^2$. This segmentation comprised six rows in depth and three columns vertically with respect to the beam, as shown in Fig. 6. Acrylic light guides having a square profile and with a 45° mirrored surface channelled the light from the fibres to the PMTs that were placed perpendicularly to the fibre direction on both the North and South ends of the module, as shown in Fig. 7. The staggered, vertical placement of the PMTs was due to their diameter of 5 cm being larger than the 3.81 cm width of the read-out segment size. Large, rectangular silicone sheets, 2.5 mm thick, were used to interface the light guides with the module and smaller, circular, 2.5 mm thick, silicone cookies coupled the PMTs to the light guides. The read-out ends and all their components were enclosed in an aluminum box painted black with the top covered by Tedlar^{®3} PVF to maintain light-

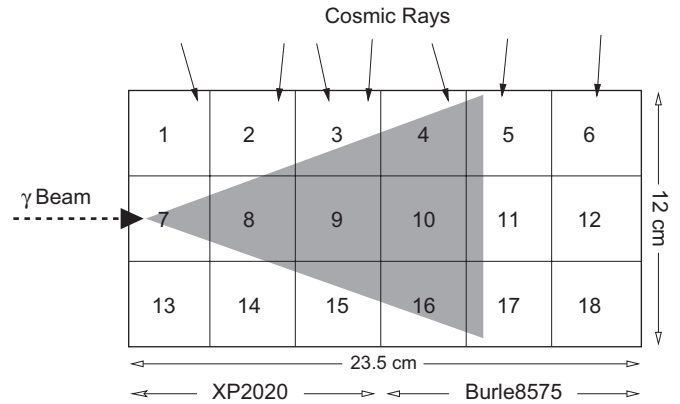


Fig. 6. The segmentation and readout for the BCAL module as viewed from its North end. The lead/scintillating-fibre matrix would appear to be rotated by 90° with respect to Fig. 4. The electromagnetic shower that develops in the module approximately forms a cone shape and is illustrated with the shaded triangle in the figure. A very small percentage of the energy is deposited in the outer segments or leaks out the sides.

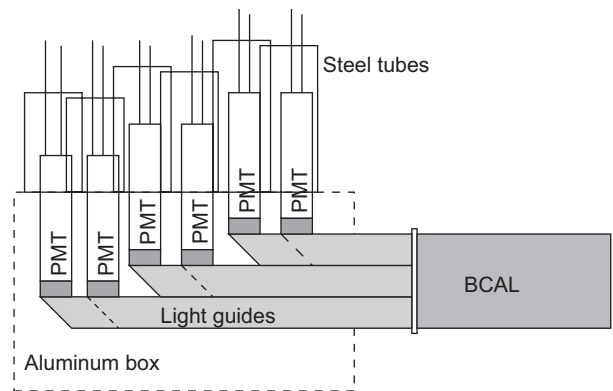
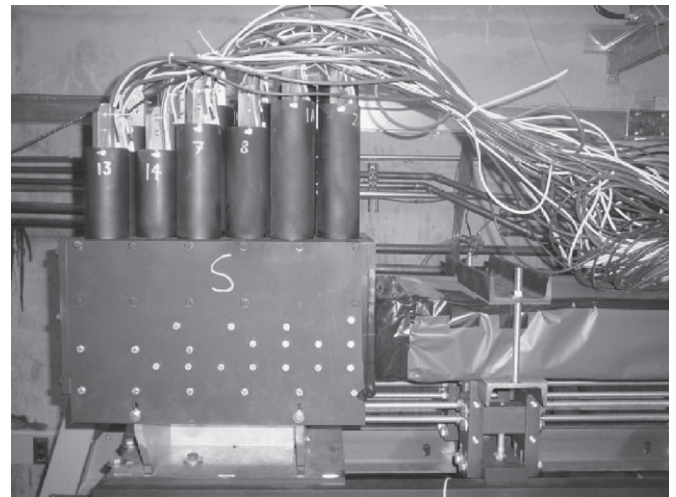


Fig. 7. The box that encloses the 18 light guides and PMTs with cables attached for the South end of the BCAL module is shown. The module is entirely wrapped in Tedlar[®] on the right and pressed against the light guides using a silicone sheet, as described in the text.

tightness. The shower profile was such that most of the energy, nearly 90%, was deposited in the first 12 cm of the BCAL and the largest number of photoelectrons originated in that part of the module. For this reason, the three upstream columns of Fig. 6

³ Tedlar[®] is a registered trademark of E. I. du Pont de Nemours and Company or its affiliates.

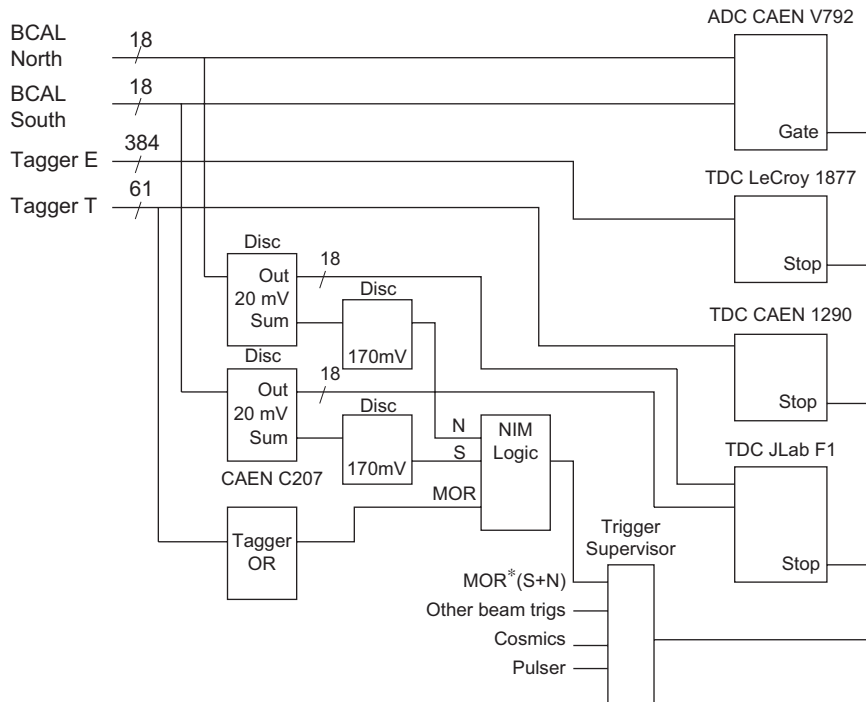


Fig. 8. The logic diagram for the BCAL Hall-B beam test electronics. It should be noted that segments 1 and 13 did not contribute to the trigger, and this explains the apparent discrepancy between the 18 outputs of the discriminator and the sum output (that is just 16).

were read out using Philips⁴ XP2020 photomultiplier tubes. These tubes were selected for their good timing characteristics. The last three rows were read out using Burle⁴ 8575 PMTs.

The bases for the PMTs were designed with dual BNC outputs on the anode. The signals were sent to a CAEN C207 equivalent leading edge discriminator and from there they were sent directly to a JLab F1 TDC [16] that was used to record the timing of the signals. The sum of the discriminator outputs was sent to a second discriminator, the threshold of which was set to require signals from at least four PMTs from each end of the module. The threshold logic pulse from either end (North or South) of the module and the Master OR (MOR) signal from the T-counters of the tagger defined the trigger for the experiment. On average, the event rate was between 1 and 4 kHz for the duration of the beam test. A special electronics module was used to allow cosmic event triggers from scintillator paddles placed above and below the module as well as triggers from a pulser that were used to establish ADC pedestals, and were recorded concurrently with beam data. Signal amplitudes from the second BNC output of the PMTs were digitized using CAEN V792 ADCs. The complete logic diagram is shown in Fig. 8.

4. Energy resolution

4.1. Gain balancing and energy calibration

With the module divided into 18 segments on each of the North and South sides, 36 PMTs were utilized in total. By adjusting the PMT supply voltage, an initial, relative balancing of the PMT gains was performed using cosmic data during the setup stage such that the means of the cosmic ADC spectra were nominally within 10% of a certain value; only a couple channels deviated from this value by up to a factor of two. Further adjustments to the

gains were done in software during the analysis, using the spectra collected during four dedicated cosmic runs.

By assuming that the energy deposited by cosmic rays is uniform in each segment of the BCAL, a gain balancing constant was found for each North and South segment by taking the ratio of each segment's spectra to that of one particular segment,

$$C_{N,i} = \frac{N_{ADC,i}}{N_{ADC,7}} \quad (1)$$

where $C_{N,i}$ was the balancing constant for the i th segment on the North side, each balanced with respect to $N_{ADC,7}$. The procedure was identical for the South end, anchoring with respect to $S_{ADC,7}$. Keeping in mind the attenuation length of the BCAL, $N_{ADC,7}$ and $S_{ADC,7}$ were then balanced with respect to one another. An overall energy calibration constant for the BCAL was then found by plotting the balanced ADC values vs. the tagged photon energy.

Once the BCAL was calibrated, the distribution of the difference between the reconstructed BCAL energy and the tagged photon beam energy was found. This ratio, D , is defined as

$$D = \frac{E_{BCAL} - E_{BEAM}}{E_{BEAM}} \quad (2)$$

where E_{BCAL} , the reconstructed energy in the BCAL module, is defined as

$$E_{BCAL} = K \cdot \sqrt{\left(\sum_{i=1}^{18} \frac{N_{ADC,i}}{C_{N,i}} \right) \left(\sum_{i=1}^{18} \frac{S_{ADC,i}}{C_{S,i}} \right)}. \quad (3)$$

E_{BEAM} is the photon energy measured in the tagger and K is the overall calibration constant. The reconstructed energy in the BCAL module is then the geometric mean of the balanced ADC values multiplied by K . The width of the distribution, σ_D , is the energy resolution, σ_E/E , for the module.

A plot of D vs. E_{BEAM} can be seen in Fig. 9. This shows how well the PMT gains are balanced and the energy in the BCAL is reconstructed. Although the deviations from zero are so small as to be inconsequential, typically less than 0.5%, there may be a

⁴ PHOTONIS SAS, Brive, France (www.photonis.com).

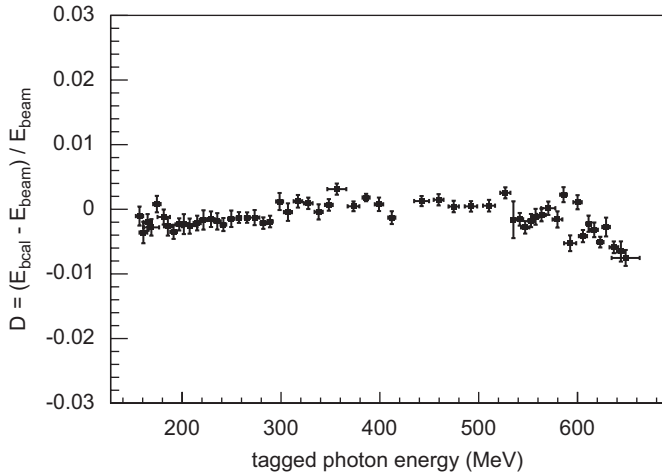


Fig. 9. $D = (E_{\text{BCAL}} - E_{\text{BEAM}})/E_{\text{BEAM}}$ is shown after gain balancing and calibration. Notice that the deviations from zero are typically less than 0.5%.

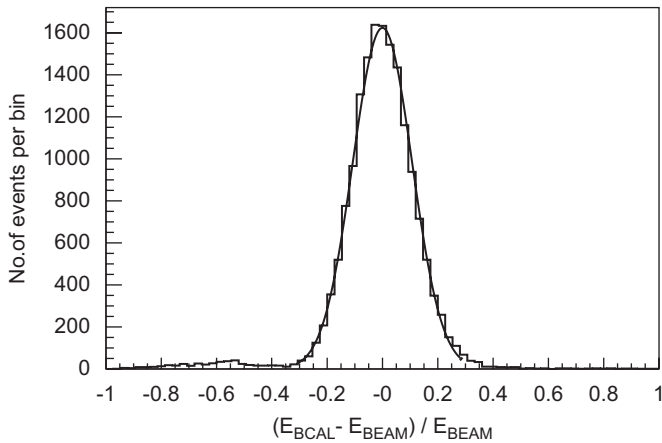


Fig. 10. The calibrated spectrum for D is shown for timing counter 40, corresponding to a beam energy of 273 MeV. The solid line is a Gaussian fit to the data.

number of physical reasons for these deviations such as non-linearities in the sampling fraction of the shower for each segment, albedo, background contributions to the ADC spectra which could not be removed at lower energies and leakage outside the module.

4.2. Energy resolution results

The calibrated spectra for D were fitted by a Gaussian function. A typical spectrum and its fit are shown in Fig. 10, this one for timing counter 40, corresponding to a beam energy of 273 MeV.

Subsequently, the energy resolution was extracted for all timing counters and is shown in Fig. 11, plotted as a function of the tagged photon beam energy, for the data at $\theta = 90^\circ$ and $z = 0$ cm. The fit to the data is also shown in Fig. 11, resulting in

$$\frac{\sigma_E}{E} = \frac{5.4\%}{\sqrt{E(\text{GeV})}} \oplus 2.3\% \quad (4)$$

where the \oplus indicates addition in quadrature. Small variations in the fits produced relatively large variations in the floor term ($2.3 \pm 1\%$) but little variation in the stochastic term ($5.4 \pm 0.1\%$).

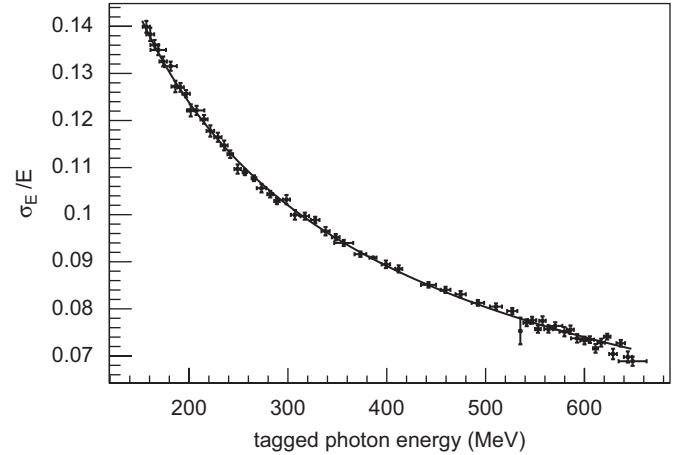


Fig. 11. Energy resolution vs. E_{BEAM} for photons for $\theta = 90^\circ$ and $z = 0$ cm. The fit gives $\sigma_E/E = 5.4\%/\sqrt{E(\text{GeV})} \oplus 2.3\%$. The fit of Fig. 10 corresponds to the 40th datum from the right (19th from the left) in this figure.

In general, the energy resolution of an electromagnetic calorimeter is expressed in the form:

$$\frac{\sigma_E}{E} = \frac{a}{\sqrt{E(\text{GeV})}} \oplus b \oplus \frac{c}{E(\text{GeV})}. \quad (5)$$

The a/\sqrt{E} term contains the combined effect of sampling fluctuations and photoelectron statistics. It is commonly referred to as the stochastic term. The $1/\sqrt{E}$ dependence is expected from the fact that the fluctuations are proportional to the number of particle tracks, n , that cross the active material; n has a Poisson distribution with a variance \sqrt{n} . Since the energy of a shower is proportional to n , the contributions to the resolution σ_E/E due to the stochastic fluctuations is proportional to $1/\sqrt{E}$. The KLOE collaboration concluded that the photon statistics from the light yield of their calorimeter ranges from $1.6\%/\sqrt{E(\text{GeV})}$ [17] up to $2.7\%/\sqrt{E(\text{GeV})}$ [18] and, therefore, contributes very little to the resolution since it is added in quadrature to the sampling contribution. Indeed, the stochastic fluctuations in sampling dominate the resolution.

The constant term, b , in Eq. (5), originates from all other energy-independent sources that contribute to uncertainties in the energy reconstruction. These sources can be mechanical imperfections, material defects, segment-to-segment calibration variations, non-uniformity of response, instability with time and shower leakage. Much work has gone into removing any of these effects during the construction of the BCAL module, throughout the beam test, and in any subsequent analysis.

If contributions from the noise term, c/E , existed, they would be from electronics noise and pileup in high-rate environments. This term increases at lower energies but has not been observed to contribute in the beam test analysis as both the rates and noise were low. Fits to the beam test data including this term produce almost identical stochastic and constant terms with values for c consistent with zero.

The stochastic coefficient $a = 5.4\%$ in Eq. (4) compares well with the corresponding ones from KLOE determined from $e^+e^- \rightarrow e^+e^-\gamma$ reconstruction, reported as $a = 5.4\%$ [3]. The KLOE beam tests [18] reported a value for $a = 5\%$. No value for b was reported in either case as it did not contribute within KLOE's energy range due to its addition in quadrature to the resolution. The KLOE calorimeter and BCAL Module 1—as read out in the beam test—have similar sampling fractions and photostatistics. Although the production read-out for BCAL will be different, the beam test setup resulted in benchmark metrics for any future upgrades to the BCAL matrix structure, such as increasing the

sampling fraction in the inner layers to improve low-energy photon detection for critical regions of exotic hybrid production phase space and producing a better energy resolution.

As mentioned above, the stochastic fluctuations in sampling dominate the resolution. This being the case, there should be little effect of the shower position along the module (z) on the energy resolution, because attenuation only affects the number of photoelectrons at the read-out ends of the module and is compensated for by the double ended read-out of the module. On the other hand, increasing the photon beam energy results in more particle tracks over a greater depth of the shower profile generated within the module, therefore more fibre layers are intercepted by more particle tracks. The expectation, then, is that the resolution will improve with increasing photon energy but remain nearly independent of the position of the beam spot. This was verified by examining the energy resolution for photon energies from 225 to 575 MeV for three z -positions at normal incidence.

Finally, b is a reasonable indicator of the intrinsic constant term in the energy resolution of the BCAL. However, the maximum energy of the photon beam test was too low to determine it precisely, as the constant term contributes negligibly to the resolution at a few hundred MeV when added in quadrature to the stochastic term. Nevertheless, since approximately 30% of the photons in GlueX will have energies above 500 MeV, efforts to minimize the constant term and extract it more accurately in future beam tests will be fruitful.

4.3. Sampling fraction and energy

The sampling fraction—the fraction of energy deposited in the SciFis—can be expressed as a ratio with respect to either the total energy deposited in the BCAL module (f) or the incident photon energy (f_γ). These quantities, however, are difficult to measure in an experiment but fairly simple to simulate. A GEANT 3.21 simulation was developed to that end, based on modelling the BCAL as a standalone package and independent from the previously mentioned simulations. Individual fibre and epoxy volumes were programmed into the Monte Carlo with the appropriate Pb:SciFi:Glue ratios and material properties resulting in the geometry shown in Fig. 4.

Simulations indicate that f_γ decreases as a function of photon energy due to leakage and this is shown in Fig. 12a, with the loss being linear above 200 MeV. It should be noted that the size of the module will primarily affect only f_γ in the sense that a smaller module will result in a smaller f_γ due to energy from the electromagnetic shower leaking outside the module. On the other hand, f depends only on the energy deposited in the matrix itself and is independent of the incident photon energy or overall geometry of the module. The deviation from linearity at low energy is probably due to the fact that more of the low-energy electrons and positrons from the electromagnetic shower stop in the lead before being sampled by the scintillating fibres. One would expect this reduction in both sampling fractions and this is what was observed.

The sampling fluctuations, σ_f/f , can be seen in Fig. 12b. These are the dominant contributor to the energy resolution, at about $4.5\%/\sqrt{E(\text{GeV})}$. Subtracting the simulated sampling fluctuation contributions from the measured energy resolution yields photoelectron statistics contribution to the energy resolution of about $3.1\%/\sqrt{E(\text{GeV})}$. This is similar to the estimated value of $\sim 2.7\%/\sqrt{E(\text{GeV})}$ from a KLOE beam test [18].

5. Timing and position resolution

The time difference of the BCAL will provide position information for neutral particles, which is needed to reconstruct their

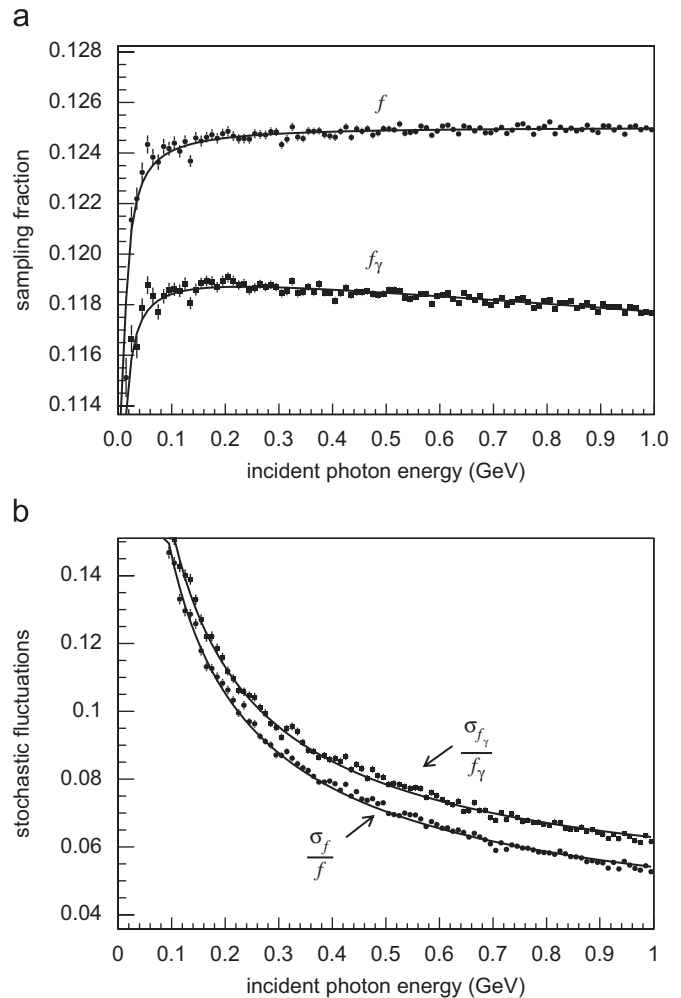


Fig. 12. (a) The photon energy sampling fraction, f_γ , and deposited energy sampling fraction, f , are shown from simulation for $\theta = 90^\circ$. The data are fit to $a_0/E + a_1E + a_2$ functions, which were chosen among the simplest functions that described the data well. (b) The sampling fluctuations of the module, $\sigma_{f_\gamma}/f_\gamma$ and σ_f/f are plotted from simulation. The data are fit to $a/\sqrt{E} \oplus b$ functions with $a_{f_\gamma} = 4.6\%$, $b_{f_\gamma} = 1.6\%$, $a_f = 4.5\%$ and $b_f = 0.9\%$.

four-momentum. The position resolution is related to the time difference resolution by the effective speed of light within the calorimeter. Thus, by using measurements of the effective speed of light ($c_{\text{eff}} = (16.2 \pm 0.4) \text{ cm/ns}$ in Table 1) from a previous beam test at TRIUMF [10], the position resolution of the calorimeter can be easily extracted.

The time difference resolution will be of the form:

$$\sigma_{\Delta T/2} = \frac{c}{\sqrt{E(\text{GeV})}} \oplus d. \quad (6)$$

In general, the constant term, d , in Eq. (6) is a result of residual calorimeter miscalibrations, but some fraction is also due to the finite width in z of the beam, which will contribute to the time difference resolution. With the beam width being $l \sim 1.9 \text{ cm}$, the flat and square distribution of the beam contributes $(l/c_{\text{eff}})/\sqrt{12} = 30 \text{ ps}$ to the resolution.

The double-ended read-out of the BCAL allowed for time difference measurements to be made, but because leading edge discriminators were used the timing had a dependence on pulse height which required a time-walk correction. A plot of ADC vs.

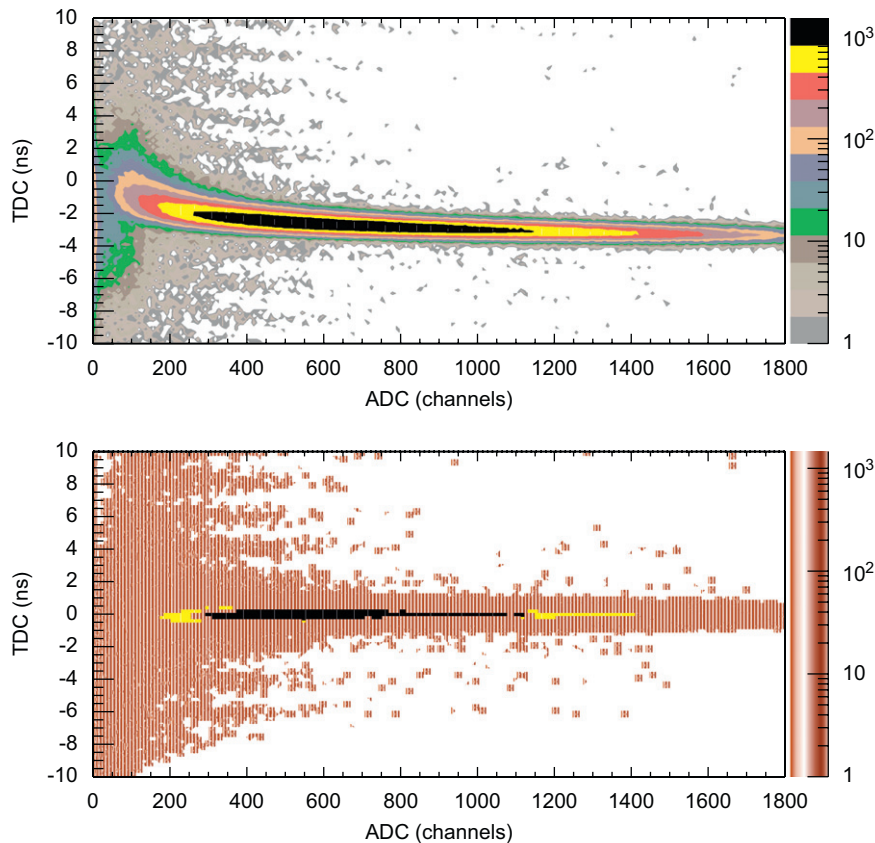


Fig. 13. ADC vs. TDC for segment South 8. The uncorrected time affected by the time walk due to the dependence on amplitude is seen in the top plot. The bottom plot shows the corrected time. The BCAL time was referenced with the tagger time (colour online).

TDC for segment 8 can be seen in Fig. 13. Fits with a function of the form $p_0/\sqrt{\text{ADC}} + p_1$ were performed, as the time delay due to signal amplitude in leading edge discriminators follows this form. The fit parameter p_1 is a constant term indicating the timing offset of the particular read-out segment from the tagger MOR timing signal. Parameter p_0 also varies depending on the particular read-out segment but has a nominal value of $\sim 35 \text{ ns GeV}^{1/2}$. The fit is poor for the downstream segments, specifically segments 6 and 18 where the statistics are low, as there is very little energy deposited there and the fluctuations are consequently large. For this reason, most of the outer segments were not included in the timing analysis. Analysis of the timing data focused mainly on segments 7, 8, 9 and 10 where nearly 90% of the energy was deposited. ADC values lower than channel 350 were rejected, in the case of South 8, due to the resulting asymmetry from the walk correction at low ADC values, which caused distortions in the time difference resolution. This corresponds to 1 MeV of energy deposited in the segment or 0.125 MeV deposited in the fibres. Similar ADC cuts were made for the other segments depending on the distortion at the lower end of the ADC spectra. This results in a loss of efficiency at the lower energies but in a much improved time difference resolution over the whole tagger spectrum.

The timing for an event was found by summing the TDC values of all the segments in an event cluster, weighted by their energy; cuts on the ADC and timing determined whether a segment was included in the cluster. A cluster is defined by the energy weighted sum of the times of each segment such that the time difference, ΔT , is expressed as

$$\frac{\Delta T}{2} = \frac{1}{2} \frac{\sum_i E_i (T_{N,i} - T_{S,i})}{\sum_i E_i}. \quad (7)$$

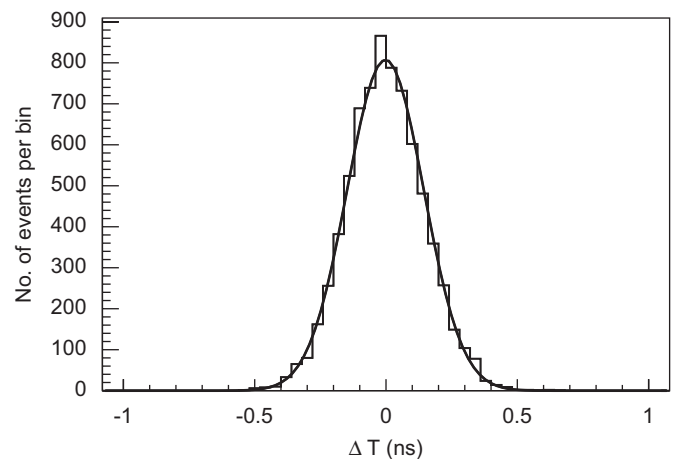


Fig. 14. The walk-corrected spectrum and Gaussian fit for timing counter 40. The solid line is a Gaussian fit to the data.

Subsequently, the walk-corrected spectra for each tagger timing counter were fitted by a Gaussian function. A typical spectrum and fit are shown in Fig. 14, this one for timing counter 40. All timing counter spectra were fitted in the same fashion, and the fit results are plotted in Fig. 15. From the subsequent fit in that figure, the time difference resolution including only the middle row segments 7, 8, 9 and 10 is found to be

$$\sigma_{\Delta T/2,7-10} = \frac{75 \text{ ps}}{\sqrt{E(\text{GeV})}} \oplus 30 \text{ ps}. \quad (8)$$

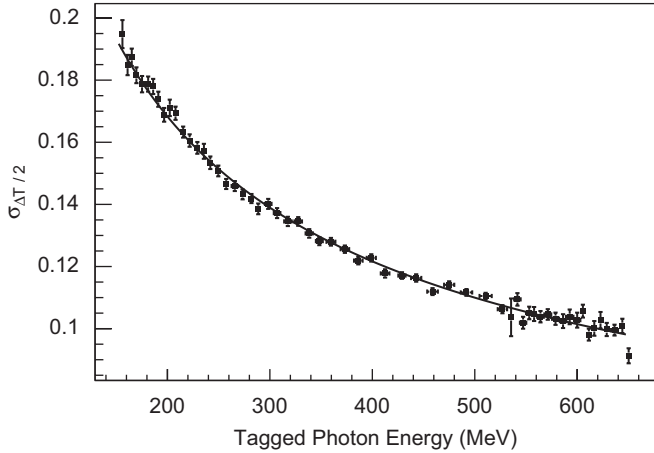


Fig. 15. The time difference resolution, in nanoseconds, for segments 7, 8, 9 and 10 as a function of energy. The fit gives $\sigma_{\Delta T/2} = 75 \text{ ps}/\sqrt{E(\text{GeV})} \oplus 30 \text{ ps}$. The fit of Fig. 14 corresponds to the 40th datum from the right (19th from the left) in this figure.

The floor term is equal to the finite width of the beam, as expected. This implies that the intrinsic time resolution of the BCAL is consistent with zero for the constant term. As the time difference resolution is dependent on the number of photoelectrons, the time difference resolution, $\sigma_{\Delta T/2,7-10}$, can be corrected to include the missing photoelectrons, after subtracting the beam width from the constant term, and is found to be

$$\sigma_{\Delta T/2} = \frac{70 \text{ ps}}{\sqrt{E(\text{GeV})}}. \quad (9)$$

The KLOE beam test result of $72 \text{ ps}/\sqrt{E(\text{GeV})}$ [18] represents the timing resolution extracted from the signal average of both ends of each segment. With better fibres and PMTs KLOE estimated they could achieve a resolution of $\sim 58 \text{ ps}/\sqrt{E(\text{GeV})}$ and this was achieved [3]. The result shown here from the BCAL beam test was extracted from the time difference of the signals. It should be noted that old/degraded PMTs were used in this beam test, especially the 18 Bule 8575s used in the three rear layers of the module, which had a timing resolution per pair averaging around 1.4 ns in contrast to the forward XP2020s that averaged around 0.6 ns per pair. As such, it is expected that the time difference resolution from Module 1 is actually better than reported here and better fibres, light guides and light sensors will result in an improved timing resolution.

Finally, the time difference resolution defines the position (z) resolution along the length of the module, since $\sigma_z = \sigma_{\Delta T/2} \cdot c_{\text{eff}}$. Therefore, the determined position resolution is calculated to be $\sigma_z = 1.1 \text{ cm}/\sqrt{E(\text{GeV})}$ for a 1 GeV photon. KLOE reported a similar position resolution from their beam test of $\sigma_z = 1.2 \text{ cm}/\sqrt{E(\text{GeV})}$ [18].

6. Determination of the number of photoelectrons

The number of photoelectrons per end of the prototype BCAL module, N_{pe} , was estimated at $z = 0 \text{ cm}$ and $\theta = 90^\circ$. The distribution in the ratio, R , of the North to the South read-out sums, for each of 10 bins in beam energy, E_j , from 150 to 650 MeV, was expressed as

$$R(E_j) = \frac{\sum_{i=1}^{18} E_{N,i,j}}{\sum_{i=1}^{18} E_{S,i,j}} \quad (10)$$

where $E_{N,i}$ and $E_{S,i}$ are the calibrated energies corresponding to the i th segment on the North and South side, respectively. Using this ratio results in the suppression of shower fluctuations that dominate the statistical variance of the individual sums for each read-out end. Under the assumption that each of the amplitude spectra has a Poisson-type shape, the ratio spectra were fitted to the function:

$$f(r) \sim \int P(x, N_{\text{pe}} \cdot \sqrt{R}) \cdot \frac{1}{r} P\left(\frac{x}{r}, \frac{N_{\text{pe}}}{\sqrt{R}}\right) \left[\frac{x}{r} dx\right] \quad (11)$$

where r is a North/South amplitude ratio, R is an average North/South amplitude ratio, N_{pe} is the average number of photoelectrons, and P is a Poisson-type probability:

$$P(x, N) = \frac{e^{-N} N^x}{\Gamma(x+1)}. \quad (12)$$

The $(1/r)$ and (x/r) factors are needed to perform the integration over the uniform r -bins. The χ^2/ndf was nearly one for all the fits. The resulting photoelectron yield per GeV per end is plotted in Fig. 16 as a function of beam energy.

The one parameter fit in Fig. 16 yields a mean value of ~ 660 photoelectrons per GeV for photons over the energy range of the beam test. A non-linearity of $\sim 5\%$ is apparent but is not worrisome due to the preliminary nature of the beam test. A similar effect can be seen in results from KLOE beam tests for photons and positrons [17]. The non-linearity in the number of photoelectrons observed may be due to the non-linearity of the detector when sampling the soft photons of an electromagnetic shower, variations in the light guides and their couplings and shower leakage. Nevertheless, this is an adequate estimation of the number of photoelectrons from this work and future beam tests over a wider range of energies with a more sophisticated read-out system similar to the final experiment will solidify this value and more thoroughly reveal any non-linearities in the detector response.

In comparison, KLOE reported $N_{\text{pe}} \sim 700$ per end at 1 GeV. The BCAL module used double-clad scintillating fibres, potentially giving rise to approximately 50% more photoelectrons than KLOE. However, the KLOE calorimeter had light guides combined with Winston Cone collectors that resulted in a much higher transport efficiency, typically $\sim 90\%$, than the light guides used in the beam tests described in this work, estimated to have a transport efficiency of $\sim 50\%$. This feature could easily compensate for the increased capture ratio of the fibres in the BCAL but lower number of measured photoelectrons.

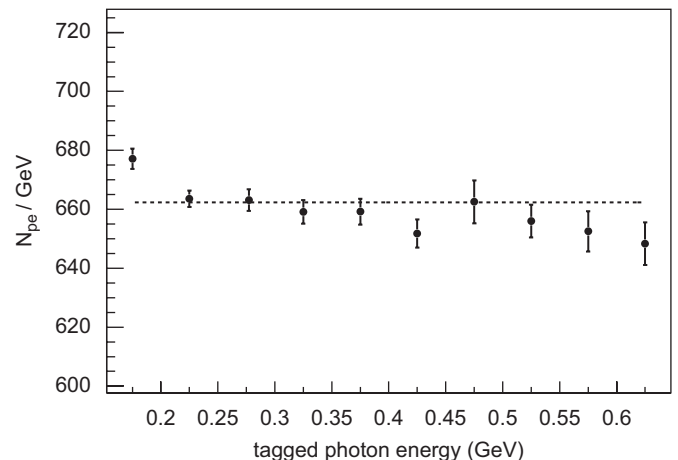


Fig. 16. The number of photoelectrons per GeV per end of the BCAL module is shown as a function of energy. A one parameter fit is plotted (dashed line). For more details see the text.

7. Summary and conclusions

The first full-scale prototype module for the BCAL tested the construction techniques and the performance of the matrix under beam conditions. An energy resolution of $\sigma_E/E = 5.4\%/\sqrt{E(\text{GeV})} \oplus 2.3\%$ and a time difference resolution of $\sigma_{\Delta T/2} = 70 \text{ ps}/\sqrt{E(\text{GeV})}$ ps were found from the Jefferson Lab beam test data. The number of photoelectrons per GeV is about 660. The energy and timing resolutions meet the original design goals and the performance of the module closely matches that of KLOE, a proven sampling calorimeter. The analysis for the more demanding regions of module and beam geometries, near the end of the module and at small incident angles can now proceed having established the performance under more benign conditions and having the Monte Carlo simulations tested and anchored to the data.

Acknowledgements

This work is supported by NSERC Grant SAPPJ-326516 and DOE Grant DE-FG02-05ER41374 as well as Jefferson Science Associates, LLC under U.S. DOE Contract no. DE-AC05-06OR23177. The authors wish to thank the Hall-B physicists and technical staff, including Doug Tilles and Dave Kashy, for their invaluable assistance in setting up and running of the beam tests and their excellent hospitality to all the GlueX personnel that occupied their Hall and counting room for nearly two weeks. Also, the authors wish to thank Tim Whitlatch and Suresh Chandra as they reviewed the safety of the beam test and made valuable suggestions. The efforts of the Accelerator and Physics Divisions at JLab were very much appreciated and contributed to the

success of the experiment. As well, the assistance, transfer of knowledge, loan of equipment and hospitality of KLOE physicists and staff towards the construction of prototype modules was both invaluable and greatly appreciated. Finally, many thanks must be given to Alex Dzierba who contributed immensely to the analysis and writing of this paper.

References

- [1] M. Adinolfi, et al., Nucl. Instr. and Meth. A 461 (2001) 344.
- [2] M. Adinolfi, et al., Nucl. Instr. and Meth. A 482 (2002) 364.
- [3] M. Adinolfi, et al., Nucl. Instr. and Meth. A 494 (2002) 326.
- [4] T. Sjöstrand, S. Mrenna, P. Skands, Pythia 6.4 physics and manual, Technical Report, Lund University, 2006.
- [5] GEANT 3.21 Detector Description and Simulation Tool, CERN Program Library Long Writeup W5013, Geneva, 1993.
- [6] R. Wigmans, Nucl. Instr. and Meth. A 494 (2002) 277.
- [7] St. Gobain Crystals, Paris, France, Scintillating Optical Fibers Brochure 605.
- [8] C.P. Achenbach, arXiv:nucl-ex/0404008v1, 2004.
- [9] Z. Papandreou, GlueX Collaboration, GlueX-doc-918-v2 (<http://portal.gluex.org/>), Documents, Public), Technical Report, 2007.
- [10] G. Koleva, GlueX Collaboration, M.Sc. Thesis (U. of Regina), 2006; GlueX-doc-824-v2, Technical Report, 2006.
- [11] Z. Papandreou, GlueX Collaboration, GlueX-doc-840-v2, Technical Report, 2007.
- [12] B.D. Leverington, GlueX Collaboration, GlueX-doc-827-v3, Technical Report, 2007.
- [13] M.J. Berger, S.M. Seltzer, Tables of energy losses and ranges of electrons and positrons, Technical Report, NASA, Washington, DC, 1964.
- [14] B. Rossi, High Energy Particles, Prentice-Hall, Inc., Englewood Cliffs, NJ, 1952.
- [15] D.I. Sober, et al., Nucl. Instr. and Meth. A 440 (2000) 263.
- [16] F.J. Barbosa, E. Jastrzembski, J. Profitt, J. Wilson, in: Nuclear Science Symposium Conference Record, vol 1, IEEE, 2002, pp. 135–139.
- [17] A. Antonelli, et al., Nucl. Instr. and Meth. A 354 (1995) 352.
- [18] A. Antonelli, et al., Nucl. Instr. and Meth. A 379 (1996) 511.